Component synergy and armor protection induced superior catalytic activity and stability of ultrathin Co-Fe spinel nanosheets confined in mesoporous silica shells for ammonia decomposition reaction

Lili Huo[a], Baocang Liu[a,b,*], Huan Li[a], Bo Cao[a], Xiu-cui Hu[c], Xin-pu Fu[c], Chunjiang Jia[c,**], Jun Zhang[a,b,*]

[a] School of Chemistry and Chemical Engineering, Inner Mongolia University, Hohhot, 010021, PR China
[b] Inner Mongolia Key Lab of Nanoscience and Nanotechnology, Inner Mongolia Engineering and Technology Research Center for Catalytic Conversion and Utilization of Carbon Resource Molecules, Inner Mongolia University, Hohhot, 010021, PR China
[c] Key Laboratory for Colloid and Interface Chemistry, Key Laboratory of Special Aggregated Materials, School of Chemistry and Chemical Engineering, Shandong University, Jinan, 250100, PR China

ABSTRACT

We report the fabrication of ultrathin Co-Fe spinel oxide nanosheets with adjustable stoichiometry confined in mesoporous SiO$_2$ shells (Co$_x$Fe$_{3-x}$O$_4$@mSiO$_2$) by encapsulating Fe-Co layered double hydroxides (FeCo-LDHs) with mesoporous SiO$_2$ shells followed with a calcination process. In this way, the unique 2D structured Co$_x$Fe$_{3-x}$O$_4$@mSiO$_2$ nanosheets offers high specific surface area and intimate contact with NH$_3$. The tunable stoichiometry of Co$_x$Fe$_{3-x}$O$_4$ nanosheets regulate the electron structure and thus optimize the nitrogen desorption ability. The encapsulation of mSiO$_2$ shells not only effectively facilitates the generation of ultrathin Co-Fe spinel oxides nanosheets with abundant active sites, but also protects Co$_x$Fe$_{3-x}$O$_4$ nanosheets from detachment and agglomeration during the NH$_3$ decomposition reaction. Benefiting from these advantages, the optimal Co$_{0.89}$Fe$_{2.11}$O$_4$@mSiO$_2$ nanosheet catalyst possesses 88% conversion of ammonia at 600 °C with a space velocity of 60 000 cm^3 g^{-1} h^{-1} and maintains even 48 h without attenuation.

1. Introduction

The excessive fossil fuel depletion and concomitant environment contamination drive the development of clean and renewable energy sources. Hydrogen is generally perceived as one of the most promising substitutes [1,2]. Ammonia (NH$_3$) has been considered as an viable hydrogen storage medium due to its unparalleled characteristics [3–5]: (i) NH$_3$ possesses the high gravimetric content of 17.8 wt% and volumetric energy density of 108 kg$_{H2}$ m^{-3} [6,7]; (ii) the transportation and storage of NH$_3$ can be handled easily since its liquefaction occurs under moderate conditions [5]; and (iii) producing hydrogen via NH$_3$ decomposition is carbon-free [8]. Therefore, NH$_3$ decomposition reaction has been regarded as a valuable venue to supply high quality hydrogen for fuel cell application [9–13]. Ru-based catalyst is the most active but its scarcity and high cost hinders its commercialization [14–16]. Earth-abundant and inexpensive transition metals, (e.g. Fe [5,17,18], Co [19,20], Ni [21,22], and Mo [10,11,23]) have been extensively studied

as potential alternatives for large-scale hydrogen production from NH$_3$. Recently, spinel AB$_2$O$_4$ oxides have heightened concerns due to their multiple valence states and the active site of A site (A^{2+}) and B site (B^{3+}) can influence each other, which will remarkably enhance the catalytic activity during the deep oxidation [24–28]. In particular, spinel CoFe$_2$O$_4$ has been explored in multiple catalytic domains but not in catalyzing NH$_3$ decomposition reaction [29–31]. Thus, fabricating well-defined spinel oxide catalysts composed of tailored nanostructures is highly desired for catalyzing NH$_3$ decomposition.

Fascinating two-dimensional (2D) layered nanomaterials have been the focus of substantial research interest owing to their special properties [32–36]. As one of the most famous 2D materials, layered double hydroxides (LDHs) nanosheets tend to form oxides, nitrides, and carbides after thermal treatment under different atmospheres, which have great potential to be applied in various catalytic reactions [37–40]. Unfortunately, there are still limitations in practical applications, especially when being applied in high-temperature catalytic reactions

like ammonia decomposition (up to 700 °C), it often encounters serious aggregation and restacking caused by the high surface energy and interlayer van der Waals force [41,42]. In view of the above-mentioned facts, it is anticipated that ultrathin mesoporous SiO_2 cladded on the surface of nanosheets may prevent nanosheets from gathering together and improve mass-transfer efficiency.

Herein, we demonstrate an approach to fabricate 2D ultrathin Co–Fe spinel oxide nanosheets encapsulated with mesoporous silica shells ($Co_xFe_{3-x}O_4@mSiO_2$) using FeCo-LDHs@SiO_2/CTAB hybrids as precursors. By tuning the stoichiometry of Co/Fe, the optimal NH_3 decomposition performance can be achieved on $Co_{0.89}Fe_{2.11}O_4@mSiO_2$ nanosheet, exhibiting as high as 88% conversion of NH_3 at 600 °C with a space velocity of 60 000 $cm^3 g^{-1} h^{-1}$ and 48 h durability without obvious attenuation owing to its unique 2D mesoporous structure.

2. Experimental section

2.1. Materials preparation

2.1.1. Synthesis of FeCo-LDHs

FeCo-LDHs were firstly prepared by a modified method described previously [43]. Briefly, 0.5 g of polyvinylpyrrolidone (PVP, MW = 53 000) was added into 10 mL 1.0 M of a mixed solution of $Fe(NO_3)_2 \cdot 9H_2O$ and $Co(NO_3)_2 \cdot 6H_2O$ with different molar ratios of 10:0, 8:2, 5:5, 2:8, and 0:10. The mixed solution was sonicated for 10 min and poured into a beaker containing 50 mL distilled water. Then, 20 mL of $NaBH_4$ solution (50 mg/mL) was added to the above solution under vigorous mechanical stirring for 6 h. Subsequently, the obtained turbid suspension was filtrated and washed by distilled water and ethanol for three times.

2.1.2. Synthesis of $Co_xFe_{3-x}O_4@mSiO_2$ hybrid nanosheets

$Co_xFe_{3-x}O_4@mSiO_2$ hybrid nanosheets with different Co/Fe molar ratios of 10:0, 8:2, 5:5, 2:8, and 0:10 were prepared via a cost efficient and simple method. Typically, 30 mg of FeCo-LDHs were dissolved in 20 mL of distilled water, then 36 mL of CTAB aqueous solution (12 mg mL^{-1}) was added and stirred at 40 °C for 0.5 h. Afterwards, 0.825 mL of TEOS was added and continuously stirred for 12 h. The solid was centrifuged and washed with deionized water before calcination at 600 °C for 3 h in air (ramp rate 2 °C min^{-1}). The bulk $Co_{0.89}Fe_{2.11}O_4$ catalyst was synthesized by directly calcining FeCo-LDHs with the Co/Fe molar ratio of 2:8 at 600 °C for 3 h. $Co_xFe_{3-x}O_4@mSiO_2$ catalysts are prepared following the similar process as those of $Co_xFe_{3-x}O_4@mSiO_2$ but with the mass ratios of FeCo-LDHs and TEOS fixed at 2:1, 1:1 and 1:2.

2.2. Materials characterization

XRD was performed on a PANalytical Empyrean diffractometer with Cu Kalpha1 radiation (λ = 1.54178 Å) in the Bragg angle ranging between 10° and 80°. Transmission electron microscopy (TEM) characterizations were performed on a FEI Tecnai F20 field-emission transmission electron microscope (FE-TEM). The scanning electron micrographs (SEM) were recorded with a HITACHI S4800 field-emission scanning electron microscope (FE-SEM). Surface area measurements were performed on an ASAP 2020 Brunauer–Emmett–Teller (BET) analyzer. X-ray photoelectron spectroscopy (XPS) was carried out on a ThermoESCALABXi$^+$. The iron and cobalt auger lines were subtracted in Co 2p and Fe 2p XPS spectra, respectively.

Temperature-programmed desorption of N_2 (N_2-TPD) was measured on a chemisorption instrument with an online mass spectrometer. Before the N_2-TPD analysis, 1.0 g of the catalysts was pre-treated at 600 °C for 30 min and then cooled to room temperature under NH_3 flow at a flow rate of 30 mL min^{-1}. Afterwards, the flow was switched to He and purged with the same flow for 1 h. Finally, the TPD signal for fragment species of m/z = 17 was recorded in the temperature range from 20 to 800 °C at a rate of 10 °C min^{-1} in a He flow.

2.3. Catalytic activity measurements

NH_3 decomposition measurements were carried out on a fixed-bed quartz tubular flow reactor with an inner diameter of 6 mm using a flow of pure NH_3. Typically, 50 mg of catalysts were loaded and heated every 10 °C from 350 to 600 °C and each temperature stabilized for 60 min under pure NH_3 at a flow rate of 19 mL min^{-1}. The effluents of N_2 and NH_3 concentrations were analysed by an online gas chromatograph equipped with a thermal conductive detector and a Porapark Q column using H_2 as the carrier gas. Steady state stability tests were also performed in the same equipment at 600 °C for 48 h with gas hourly space velocity of 60 000 $cm^3 g_{cat}^{-1} h^{-1}$. The apparent activation energy for NH_3 decomposition was measured using a fixed conversion of 12.5% by tuning the reaction temperature (380–460 °C) and the space velocity (9000–36 000 $cm^3 g_{cat}^{-1} h^{-1}$).

3. Results and discussion

3.1. Synthesis and structure of $Co_xFe_{3-x}O_4@mSiO_2$ catalysts

3.1.1. Synthesis process

The fabrication procedures of $Co_xFe_{3-x}O_4@mSiO_2$ are schematically illustrated in Scheme 1. Initially, FeCo-LDHs were synthesized via a simple co-precipitation method using metal cobalt and iron salts as precursors, polyvinylpyrrolidone (PVP) as modulating agent, and $NaBH_4$ as strong reductant, followed with the hydrolysis of tetraethyl orthosilicate (TEOS) to form mesoporous SiO_2 shells on surface of FeCo-LDHs using CTAB as a pore-generating agent. Finally, the $Co_xFe_{3-x}O_4@mSiO_2$ nanosheets were obtained by annealing the resulting products at 600 °C under air atmosphere. For convenience, the $Co_xFe_{3-x}O_4@mSiO_2$ catalysts with different Co/Fe molar ratios were denoted as $Fe_2O_3@mSiO_2$, $Co_{0.89}Fe_{2.11}O_4@mSiO_2$, $Co_{1.67}Fe_{1.33}O_4@mSiO_2$, $Co_{2.52}Fe_{0.48}O_4@mSiO_2$, and $Co_3O_4@mSiO_2$, as determined by EDS measurement (Table S1), respectively.

3.1.2. Phase structure, morphology, and 2D configuration

Fig. 1a displays XRD patterns of $Co_xFe_{3-x}O_4@mSiO_2$ catalysts with variable Co/Fe molar ratios. The characteristic diffraction peaks of $Fe_2O_3@mSiO_2$ are consistent with hematite α-Fe_2O_3 (JCPDS No. 85-0599), while the $Co_3O_4@mSiO_2$ belong to spinel Co_3O_4(JCPDS No. 74-1656). The diffraction peaks of bimetallic $Co_xFe_{3-x}O_4@mSiO_2$ catalysts are associated with cubic $CoFe_2O_4$ (JCPDS No. 03-0864) [44]. According to the Scherrer equation, the particle size of $Fe_2O_3@mSiO_2$, $Co_{0.89}Fe_{2.11}O_4@mSiO_2$, $Co_{1.67}Fe_{1.33}O_4@mSiO_2$, $Co_{2.52}Fe_{0.48}O_4@mSiO_2$, and $Co_3O_4@mSiO_2$ catalysts is estimated to be 8.1, 5.6, 5.0, 6.5 and 7.8 nm, respectively. SEM images (Fig. 1b–f) show uniform flower-like nanosheets can be found in $Co_xFe_{3-x}O_4@mSiO_2$ with low Co/Fe molar ratios (x < 1.0) and the size of nanosheets is variable from several hundred nanometers to a few microns. However, with the increasing of Co content, the density of $Co_xFe_{3-x}O_4@mSiO_2$ catalysts are gradually reduced and even aggregated into large and thick nanosheets. The morphological differences of $Co_xFe_{3-x}O_4@mSiO_2$ catalysts with variable Co/Fe molar ratios may root in different zeta potentials of FeCo-LDHs surface, which may influence the assembled behavior of SiO_2/CTAB hybrid shells [40]. The elemental mapping analysis reveals that the $Co_{0.89}Fe_{2.11}O_4@mSiO_2$ catalyst owns a uniform distribution of Fe, Co, Si and O, indicating a heterostructure coupling of Co-Fe spinel oxides nanosheets and mesoporous SiO_2 shells.

TEM measurements were carried for further insight into the detailed microstructure of $Co_xFe_{3-x}O_4@mSiO_2$ catalysts. The $Co_{0.89}Fe_{2.11}O_4@mSiO_2$ display that the twisted and wrinkled nanosheets with a thickness of less than 10 nm (Fig. 2a–c). However, the irregular and overlapped lamellar structure can be detected in $Co_{1.67}Fe_{1.33}O_4@mSiO_2$ and $Co_{2.52}Fe_{0.48}O_4@mSiO_2$ catalysts (Figures S1a-c and S2a-c), implying that the adhesion between mesoporous SiO_2 shells and $Co_xFe_{3-x}O_4$ nanosheets gradually weakens with the increase of Co content. In addition, the abundant mesopores with an average size of ~3 nm disperses over the nanosheets, forming a sandwich-like structure (Figs. 2c, S1d
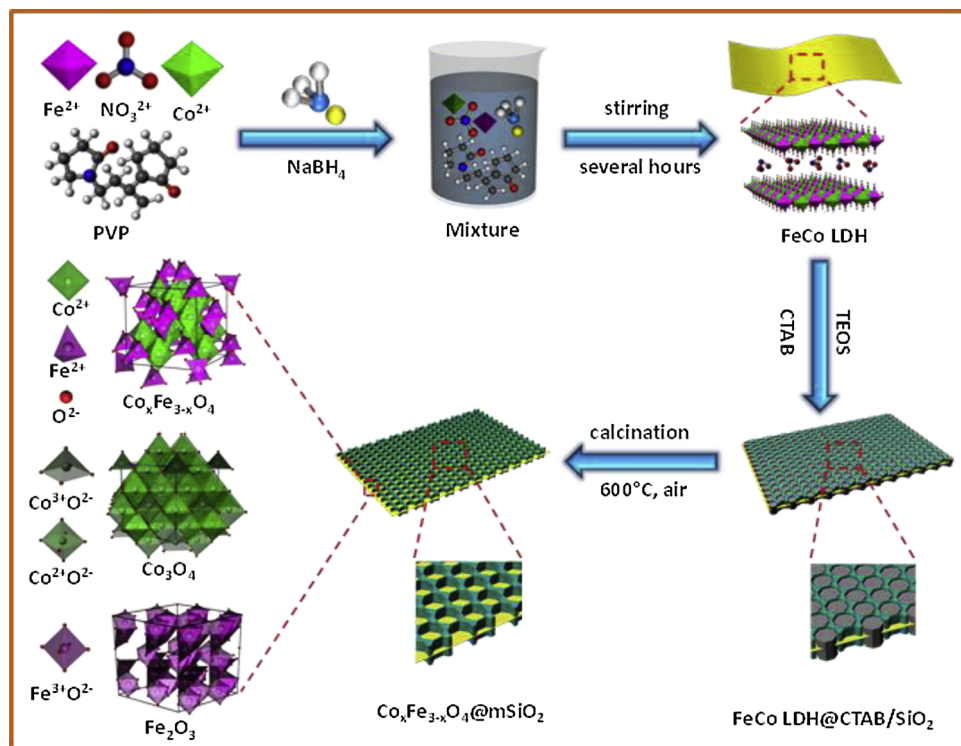
Scheme 1. Schematic illustration shows the synthetic process of $Co_xFe_{3-x}O_4@mSiO_2$ catalysts.

and S2d) [42]. SAXRD patterns of $Co_xFe_{3-x}O_4@mSiO_2$ catalysts show no diffraction peaks can be observed, indicating the existence of disordered mesoporous silica structures (Figure S3). The HRTEM image of

$Co_{0.89}Fe_{2.11}O_4@mSiO_2$ nanosheet reveals well-resolved lattice fringes with interplanar distances of 0.198 and 0.167 nm, corresponding to the (311) and (220) planes of $CoFe_2O_4$, respectively (Fig. 2d) [44]. The
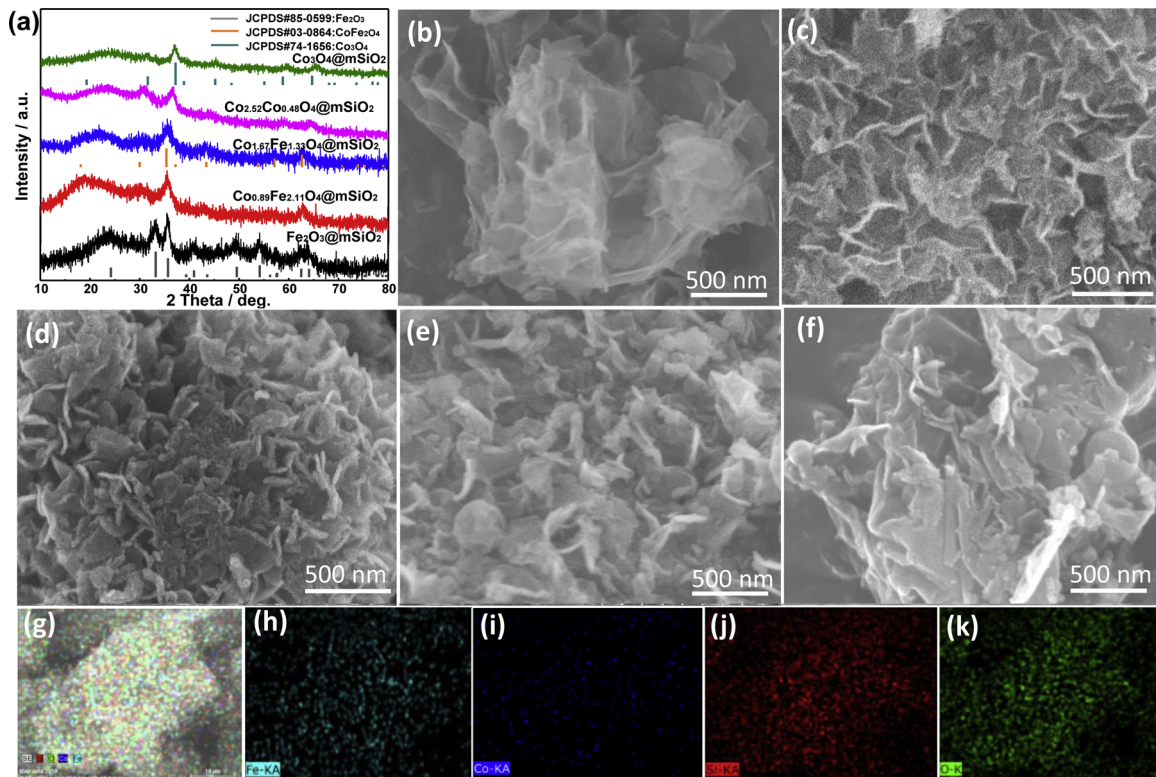
Fig. 1. (a) XRD pattern of $Co_xFe_{3-x}O_4@mSiO_2$ catalysts with different molar ratios of Co/Fe; SEM images of (b) $Fe_2O_3@mSiO_2$, (c) $Co_{0.89}Fe_{2.11}O_4@mSiO_2$, (d) $Co_{1.67}Fe_{1.33}O_4@mSiO_2$, (e) $Co_{2.52}Fe_{0.48}O_4@mSiO_2$, and (f) $Co_3O_4@mSiO_2$ catalysts; EDX elemental mapping of (g) overlap, (h) Fe, (i) Co, (j) Si, and (k) O in $Co_{0.89}Fe_{2.11}O_4@mSiO_2$ catalyst.
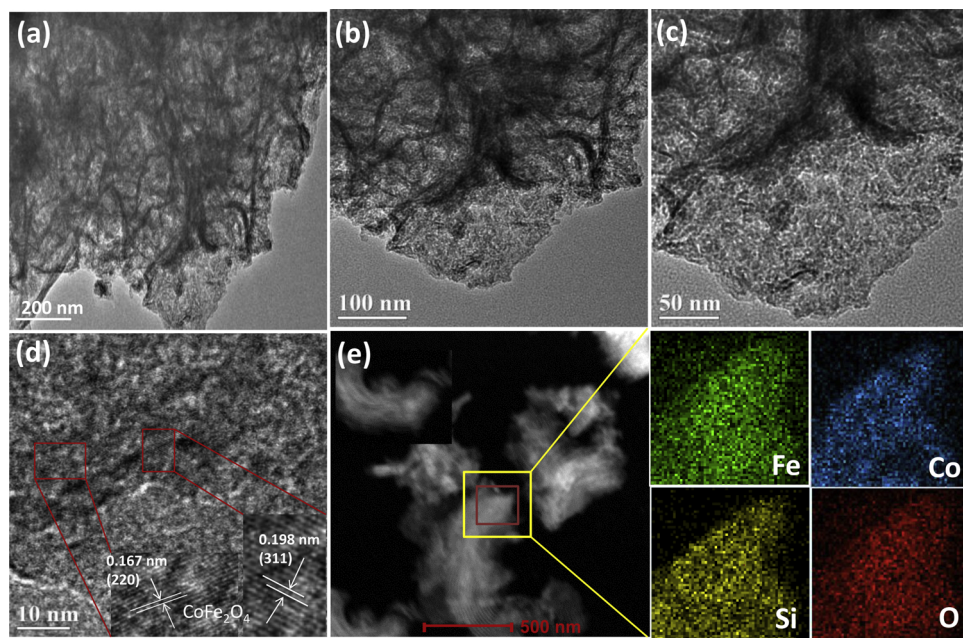
**Fig. 2.** (a–c) TEM, (d) HRTEM, (e) STEM images the corresponding EDX elemental mapping images of Fe, Co, Si, and O in $Co_{0.89}Fe_{2.11}O_4@mSiO_2$ catalyst.

HAADF-STEM images and corresponding EDX elemental mapping images show that Fe, Co, Si, and O elements are evenly distributed within the $Co_{0.89}Fe_{2.11}O_4@mSiO_2$ nanosheets (Fig. 2e).

3.1.3. Specific surface area and porous property

N_2 adsorption–desorption technique was employed to assess the specific surface area and porous feature of $Co_xFe_{3-x}O_4@mSiO_2$ catalysts. All $Co_xFe_{3-x}O_4@mSiO_2$ catalysts showing a typical IV isotherm with an H1 hysteresis loop confirm the existence of mesopores [45] and average pore diameter centered at around 2.5 nm (Fig. 3). The specific surface area of $Co_xFe_{3-x}O_4@mSiO_2$ catalysts gradually decreases with the increasing of Co contentowing to their progressively thickenedand overlapped lamellar structure (Table S2). The bulk $Co_{0.89}Fe_{2.11}O_4$ catalyst shows a typical type II isotherm with an H2 hysteresis, hinting its nonporous characteristic (Figure S4).

3.2. Catalytic performance of NH_3 decomposition

The NH_3 decomposition performance of a series of $Co_xFe_{3-x}O_4@mSiO_2$ catalysts was investigated at a space velocity of 22800 cm^3 $g_{cat}^{-1}h^{-1}$ (Fig. 4a). The activity in terms of NH_3 conversion is highly dependent on the composition of $Co_xFe_{3-x}O_4@mSiO_2$ catalysts and bimetallic $Co_xFe_{3-x}O_4@mSiO_2$ exhibits the higher NH_3 conversion than

monometallic catalysts. Considering that the specific surface area is gradually decreased with the addition of Co, the enhanced catalytic activity should be originated from the increase of intrinsic activity due to the synergistic effect between Fe and Co atoms [26]. Impressively, when the Co/Fe atomic ratio of ∼ 1:2 is offered, the NH_3 conversion achieves a maximum and nearly full conversion at temperatures as low as 550 °C.

Fig. 4b displays NH_3 conversion rate normalized by the specific surface areas at 450 °C, in which the bimetallic spinel oxides displayed superior catalytic activity to the monometallic oxides. This indicates that the construction of bimetallic spinel oxides can improve the intrinsic activity. The turnover frequency (TOF) for each active site is estimated to understand the intrinsic activity of $Co_xFe_{3-x}O_4@mSiO_2$ with Co/Fe mole ratios ion (See the Supporting Information for the detailed calculation process). As seen in Fig. 4b and Table 1, the TOF values for bimetallic spinel oxides are higher than those of two monometallic oxides. It can be deduced that the Fe atoms partially replaced by Co atoms on an atomic scale in spinel structure have excellent intrinsic activity due to the strong coupling effects between Fe and Co atoms. Moreover, the $Fe_2O_3@mSiO_2$ shows the smaller TOF of 0.037 s^{-1} compared to that of $Co_3O_4@mSiO_2$ (0.062 s^1), proving the intrinsic catalytic activity of Fe metal is inferior to Co metal in NH_3 decomposition reaction. To verify the effect of gas diffusion on activity, we
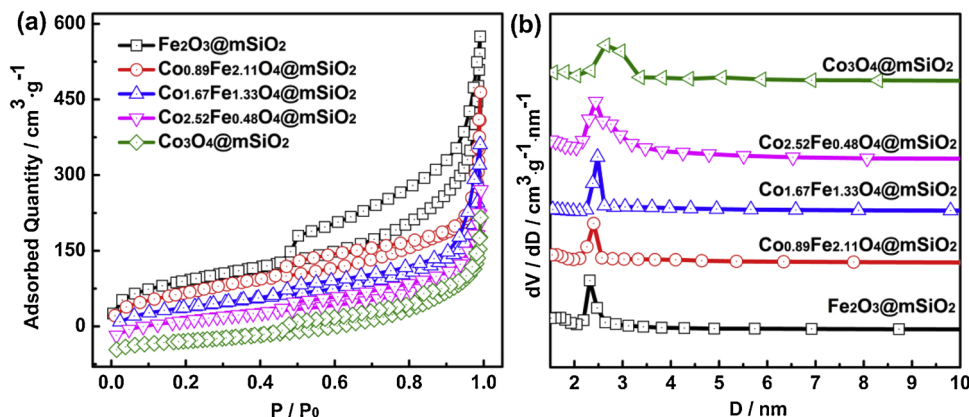

Fig. 3. (a) N_2 adsorption/desorption curves and (b) pore size distribution of $Co_xFe_{3-x}O_4@mSiO_2$ catalysts with different molar ratios of Co/Fe.
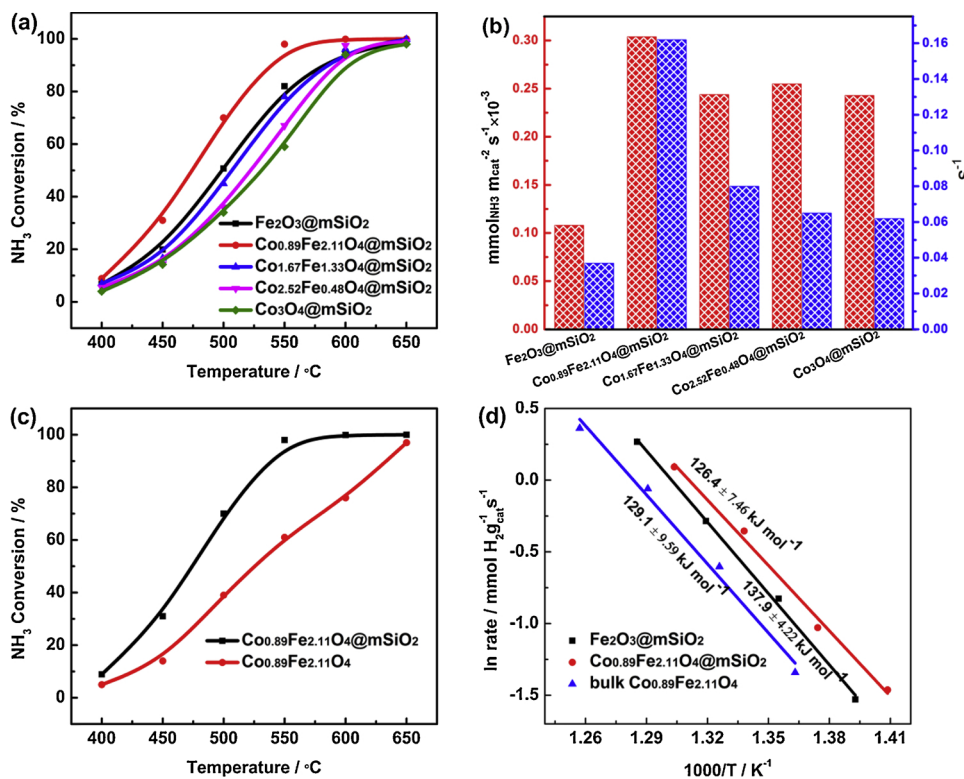
Fig. 4. (a) Temperature-dependent NH_3 decomposition, (b) the NH_3 conversion rate normalized by the specific surface area of catalysts (red) and TOFs (blue) at 450 °C over Fe_2O_3@$mSiO_2$, $Co_{0.89}Fe_{2.11}O_4$@$mSiO_2$, $Co_{1.67}Fe_{1.33}O_4$@$mSiO_2$, $Co_{2.52}Fe_{0.48}O_4$@$mSiO_2$, and Co_3O_4@$mSiO_2$ catalysts at a GHSV of 22800 cm^3 g_{cat}^{-1} h^{-1}, (c) Temperature-dependent NH_3 decomposition of $Co_{0.89}Fe_{2.11}O_4$@$mSiO_2$ and bulk $Co_{0.89}Fe_{2.11}O_4$ catalysts, and (d) Arrhenius plots of Fe_2O_3@$mSiO_2$, $Co_{0.89}Fe_{2.11}O_4$@$mSiO_2$, and bulk $Co_{0.89}Fe_{2.11}O_4$ catalysts (For interpretation of the references to colour in this figure legend, the reader is referred to the web version of this article).

Table 1

Comparison of the catalytic performance of different $Co_xFe_{3-x}O_4$@$mSiO_2$ and bulk $Co_{0.89}Fe_{2.11}O_4$ catalysts for NH_3 decomposition at 450 °C.

Catalysts	NH_3 Decom. Rate ($mmol_{NH3}$ $g_{cat}^{-1}s^{-1}$)	NH_3 Decom. Rate ($mmol_{NH3}$ $m_{cat}^{-2}s^{-1}$) $\times 10^{-3}$)	Moles of active sites ($mmol$ g^{-1})	TOF (s^{-1})
Fe_2O_3@$mSiO_2$	0.056	0.108	1.53	0.037
$Co_{0.89}Fe_{2.11}O_4$@$mSiO_2$	0.089	0.304	0.55	0.162
$Co_{1.67}Fe_{1.33}O_4$@$mSiO_2$	0.047	0.244	0.59	0.080
$Co_{2.52}Fe_{0.48}O_4$@$mSiO_2$	0.042	0.255	0.65	0.065
Co_3O_4@$mSiO_2$	0.039	0.243	0.63	0.062
Bulk $Co_{0.89}Fe_{2.11}O_4$	0.036	0.297	0.24	0.150

also investigated the NH_3 decomposition performance for the $Co_{0.89}Fe_{2.11}O_4$@$mSiO_2$ catalysts with different thickness of mesoporous silica shells (Figure S5). It can be seen clearly that the $Co_{0.89}Fe_{2.11}O_4$@$mSiO_2$ catalyst with the thinnest thickness of mesoporous silica shell as illustrated by TEM (Figure S6) may generate optimal gas diffusion efficiency, and thereby exhibits the highest performance among $Co_{0.89}Fe_{2.11}O_4$@SiO_2 catalysts.

To study the effects of the microstructure on NH_3 decomposition performance, the activity of bulk $Co_{0.89}Fe_{2.11}O_4$was determined (Fig. 4c). The activity of bulk $Co_{0.89}Fe_{2.11}O_4$ is obviously lower than that of mesoporous $Co_{0.89}Fe_{2.11}O_4$@$mSiO_2$ under the identical conditions. This illustrates the improvement of activity in $Co_{0.89}Fe_{2.11}O_4$@$mSiO_2$ catalysts may be mainly attributed to strong coupling between $Co_{0.89}Fe_{2.11}O_4$ nanosheets and $mSiO_2$ shells. Furthermore, in order to further show the superior properties of these nanosheets catalysts, we synthesized three additional catalysts of Fe_2O_3/KIT-6, Co_3O_4/KIT-6 and $CoFe_2O_4$/KIT-6 with 3D mesoporous structure as characterized by XRD and TEM (Figures S7 and S8). Temperature-dependent NH_3 decomposition show that the catalytic activity of Fe_2O_3/KIT-6, Co_3O_4/KIT-6, and $CoFe_2O_4$/KIT-6 catalysts is obviously inferior to Fe_2O_3/$mSiO_2$, Co_3O_4/$mSiO_2$, and $Co_{0.89}Fe_{2.11}O_4$@$mSiO_2$ catalysts (Figure S9), further indicating 2D structured $Co_xFe_{3-x}O_4$/$mSiO_2$ catalysts exhibit unique advantages in comparison with those of 3D mesoporous catalysts due to high mass transfer efficiency and more accessible active sites.

The apparent activation energies were calculated using the Arrhenius equation ($lnk = lnA-E_a/RT$), where k is the rate value and E_a is the apparent activation energy. As presented in Fig. 4d, monometallic Fe_2O_3@$mSiO_2$ catalyst displays an E_a of 137.9 kJ mol^{-1}, while bimetallic $Co_{0.89}Fe_{2.11}O_4$@$mSiO_2$ catalyst decreases the activation energy by over 10 kJ mol^{-1}. This reveals that the formation of ternary cobalt iron spinel oxide can create new highly active sites [46]. However, the small difference in activation energy between bulk $Co_{0.89}Fe_{2.11}O_4$ (129.1 kJ mol^{-1}) and $Co_{0.89}Fe_{2.11}O_4$@$mSiO_2$ (126.4 kJ mol^{-1}) implies that they obey similar reaction pathways in NH_3 decomposition reaction. This further demonstrates that the enhanced activity of $Co_{0.89}Fe_{2.11}O_4$@$mSiO_2$ catalyst may come from the unique structural feature.

The long-term stability tests of $Co_{0.89}Fe_{2.11}O_4$@$mSiO_2$ and bulk $Co_{0.89}Fe_{2.11}O_4$ catalysts were examined at a given GHSV of 60000 cm^3 g_{cat}^{-1} h^{-1} (Fig. 5a). Distinctly, the $Co_{0.89}Fe_{2.11}O_4$@$mSiO_2$ catalyst presents a NH_3 conversion leveling off when measured at 600 °C over continuous 48 h while bulk $Co_{0.89}Fe_{2.11}O_4$ catalyst undergoes a deactivation process. Subsequently, we calculated the reaction rate normalized by the mass of catalysts during a long-term stability test at 600 °C (Fig. 5b). The bulk $Co_{0.89}Fe_{2.11}O_4$ has the lower hydrogen formation rate of 0.59 mmol g^{-1} s^{-1} than that of 2D $Co_{0.89}Fe_{2.11}O_4$@$mSiO_2$ at the end of stability test. Long-term cycling tests (Figure S10) show that the activity recorded on $Co_{0.89}Fe_{2.11}O_4$@$mSiO_2$ catalyst is basically identical with the initial value whereas bulk $Co_{0.89}Fe_{2.11}O_4$
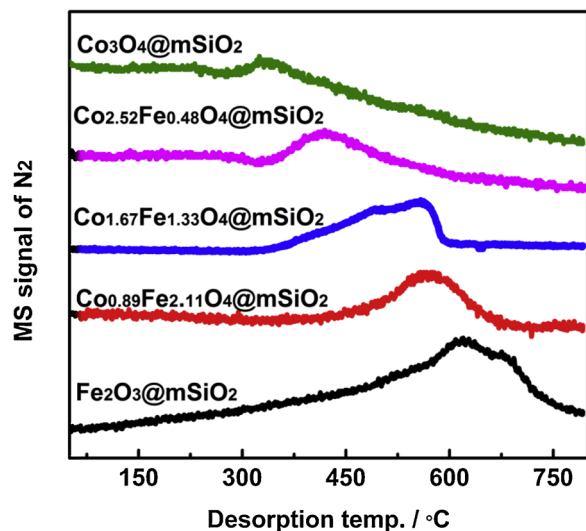
Fig. 6. N_2-TPD profiles of $Fe_2O_3@mSiO_2$, $Co_{0.89}Fe_{2.11}O_4@mSiO_2$, $Co_{1.67}Fe_{1.33}$-$O_4@mSiO_2$, $Co_{2.52}Fe_{0.48}O_4@mSiO_2$, and $Co_3O_4@mSiO_2$ catalysts.

shows a significant decrease in activity after four cycle tests. This suggests that the $Co_{0.89}Fe_{2.11}O_4@mSiO_2$ catalyst has an excellent durability even in extreme environment.

3.3. Understanding composition-dependence of catalytic activity

3.3.1. Desorption of absorbed nitrogen

The nitrogen-binding energy of transition metals (M–N) has a very significant impact on NH_3 conversion since the associative desorption of adsorbed N atoms is the rate-limiting step [47,48]. The metal-nitrogen binding energy can be reflected from the N_2 desorption temperature was evaluated by N_2-TPD. As shown in Fig. 6, the N_2 desorption temperature of $Co_xFe_{3-x}O_4@mSiO_2$ catalyst gradually reduces with the increase of Co content, implying the M−N bond strength decreases from Fe to Co. The strongest M−N bond for $Fe_2O_3@mSiO_2$ will facilitate the dissociative adsorption of NH_3 but the desorption of associative nitrogen will occur difficultly. For $Co_3O_4@mSiO_2$ with the weakest M−N bond, the dissociative adsorption of NH_3 on metals will hardly occur and thereby the intermediate species of $NH_{2,ad}$ and NH_{ad} desorb easily before further dehydrogenation, leading to low catalytic activity. The $Co_{0.89}Fe_{2.11}O_4@mSiO_2$ catalyst with a moderate M−N bond strength exhibits the highest catalytic activity.

3.3.2. Surface active species

XPS was employed to analyze the surface elemental compositions and valence states of catalysts. The high resolution XPS spectra of Fe 2p

display the dominant Fe 2p3/2 and Fe 2p1/2 characteristic peaks with the binding energies centered at 711.0 and 724.3 eV, respectively, accompanied by two shake-up satellite peaks at ca. 718.7 and 732.3 eV (Fig. 7a), confirming that the Fe species predominantly existed in the form of Fe (III) [49,50]. In the high-resolution Co 2p spectrum of $Co_3O_4@mSiO_2$, the spin–orbit splitting between the Co 2p3/2 and Co 2p1/2 is approximately 15.1 eV, which is consistent with that of Co_3O_4 [51,52]. For bimetallic $Co_xFe_{3-x}O_4@mSiO_2$ catalysts, two major peaks centered at 781.1–781.6 eV and 796.7–797.0 eV correspond to Co 2p3/2 and Co 2p1/2, respectively. The presence of the satellite peaks at around 786.5–787.9 eV and 803.1–804.5 eVconfirms that the cobalt mainly exists in the Co^{2+} state and are characteristics to spinel phase of $CoFe_2O_4$ [49,53]. Notably, the Fe $2p_{3/2}$ binding energies of bimetallic $Co_xFe_{3-x}O_4@mSiO_2$ catalysts exhibit the positive shifts while the Co^{2+} 2p3/2 signals occur negative shifts compared with those of monometallic catalyst. This implies that the charges transfer from Fe to Co and the strong electronic interaction exists between Fe and Co. Considering that the energy barrier value on metals may be affected by the electron density around metals and a appropriate electron transformation for $Co_{0.89}Fe_{2.11}O_4@SiO_2$ catalyst result in moderate M–N interaction, and thereby exhibits the highest NH_3 decomposition performance among $Co_xFe_{3-x}O_4@SiO_2$ catalysts.

3.3.3. Synergistic interaction between different components

H_2-TPR experiments were carried out to investigate the reduction behaviors and synergistic interaction between different components. The $Fe_2O_3@mSiO_2$ catalyst exhibits three apparent hydrogen consumption peaks at 401, 563, and 631 °C (Fig. 8a), which correspond to the reduction of Fe_2O_3 to Fe_3O_4, Fe_3O_4 to FeO and FeO to Fe° [5]. Compared with the H_2-TPR profile of $Fe_2O_3@mSiO_2$ catalyst, incorporating a little Co may not reshape the H_2-TPR profile but cause a shift in the peak. This can be stemmed from the presence of intimate interaction between the two reducible species Fe(III) and Co(II) as a result of generation of spinel $CoFe_2O_4$ phase in catalysts [49,55]. Notably, the $Co_{2.52}Fe_{0.48}O_4@mSiO_2$ and monometallic $Co_3O_4@mSiO_2$ only displays one reduction peak at low temperature, representing a tough emergence of active species of metallic Fe and Co and hence presenting a lower ammonia decomposition activity. Moreover, the $Co_xFe_{3-x}O_4@mSiO_2$ catalysts present identical hydrogen consumption peaks in a much higher temperature region from 700 to 900 °C, which is related to Co^{x+} and Fe^{x+} ions incorporated into the crystal lattice of silica [51,55]. The reduction peaks of bulk $Co_{0.89}Fe_{2.11}O_4$ are shifted to higher temperature compared to $Co_{0.89}Fe_{2.11}O_4@mSiO_2$ catalyst (Fig. 8b), implying that silica exerts a positive influence on the reduction of Fe(III) and Co(II) species. Moreover, the H_2-TPR profiles of bulk $Co_{0.89}Fe_{2.11}O_4$ catalyst return to the baseline in the temperature region above 800 °C. These results suggest the existence of a strong interaction between Fe and Co active species and mesoporous silica, which will contribute to the enhancement of catalytic activity.
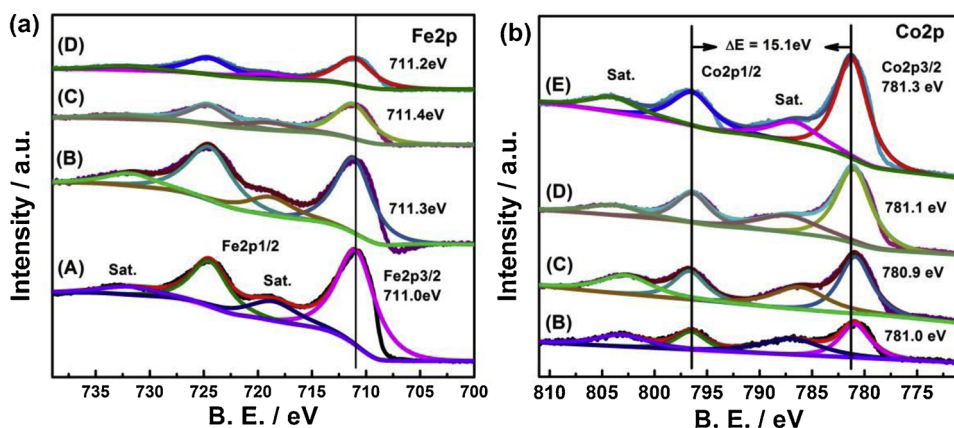
Fig. 7. High-resolution XPS spectra of (a) Fe 2p and (b) Co 2p of (A) $Fe_2O_3@mSiO_2$, (B) $Co_{0.89}Fe_{2.11}O_4@mSiO_2$, (C) $Co_{1.67}Fe_{1.33}O_4@mSiO_2$, (D) $Co_{2.52}Fe_{0.48}O_4@mSiO_2$, and (E) $Co_3O_4@mSiO_2$ catalysts.

3.4. Structural stability of $Co_xFe_{3-x}O_4@mSiO_2$ catalysts

The microstructure of $Co_xFe_{3-x}O_4@mSiO_2$ catalysts after the catalytic reaction was characterized by TEM. Clearly, $Co_xFe_{3-x}O_4$ nanosheet is completely transformed into nanoparticles with an average size of ca. 3–10 nm and these nanoparticles are well encapsulated in mesoporous SiO_2 layers (Figs. 9 and S12). The HRTEM images display the interplanar distance of ˜0.238 nm corresponding to the (011) planes of hexagonal Fe_2N and a lattice spacing of 0.246 nm ascribed to the (110) plane of cubic CoFe alloy (Fig. 9i). These interplanar distances are in good agreement with XRD data of the used $Co_xFe_{3-x}O_4@mSiO_2$ (Figure S13). In addition, some boundaries, defects, and dislocations due to the transformation of Fe_2N or FeCo alloy nanoparticles from $Co_xFe_{3-x}O_4$ nanosheets can be observed and they are usually considered as active sites [56]. N_2 sorption/desorption curves reveal that all the used $Co_xFe_{3-x}O_4@mSiO_2$ catalysts still possess obvious mesoporous features and average pore diameter centered at around 3.5 nm (Figure S14). However, the specific surface area of the used $Co_xFe_{3-x}O_4@mSiO_2$ catalyst sharply decreases compared with that of the fresh catalysts (Table S2). The high resolution Fe 2p and Co 2p XPS spectra demonstrate the used catalysts display the representative characteristic peaks of FeN_x (707.1/720.4 eV) and CoN_x (779.4/794.5 eV) species [57,58], further suggesting there is a phase transition for $Co_xFe_{3-x}O_4@mSiO_2$ catalysts after the ammonia decomposition reaction(Figure S15).

There are probably several reasons for the superior NH_3 decomposition performance of $Co_xFe_{3-x}O_4@mSiO_2$ catalysts. As is proposed in Scheme 2, the spinel oxides consisting of iron and cobalt cations occupying tetrahedral and octahedral gaps enrich active sites and generatean intimate interaction exists between the two active species, which greatly benefits the improvement of catalytic activity. Then, the thin 2D layered structure offers more contact areas with reactant molecules and maximizes the mass efficiency. The presence of mesoporous silica shells not only is helpful to facilitate the transport of reaction molecules, intermediates, and products, but also prevent unwanted agglomeration of active sites and provide isolated spaces for confining the formed nitride nanoparticles with specific size during the reaction, resulting in good mechanical and catalytic stability. Finally, the $Co_xFe_{3-x}O_4$ nanosheets bedecked mesoporous silica with grain boundaries, defects and dislocations are considered to be the active sites andhave higher catalytic capability. The synergy effects between $Co_xFe_{3-x}O_4$ nanosheets and mesoporous silica can further enhance the catalytic activity due to the strong bonding interaction.

4. Conclusion

In summary, 2D layered heterostructure of ultrathin Co-Fe spinel oxide nanosheets encapsulated in mesoporous SiO_2 shells have been successfully fabricated and the obtained $Co_xFe_{3-x}O_4@mSiO_2$ catalysts exhibit outstanding ammonia decomposition performance. In addition to the large specific surface area and the intimate Fe-Co interaction, the high performance also originates from unique mesoporous SiO_2 shells, which avoids the aggregation of $Co_{0.89}Fe_{2.11}O_4$ nanosheets and provides a confined space for stabilizing the formed Co-Fe nitride nanoparticles. More importantly, tuning the chemical stoichiometry of $Co_xFe_{3-x}O_4$ nanosheets can reasonably adjust the M−N bond strength and subsequently greatly optimize the catalytic performance. These
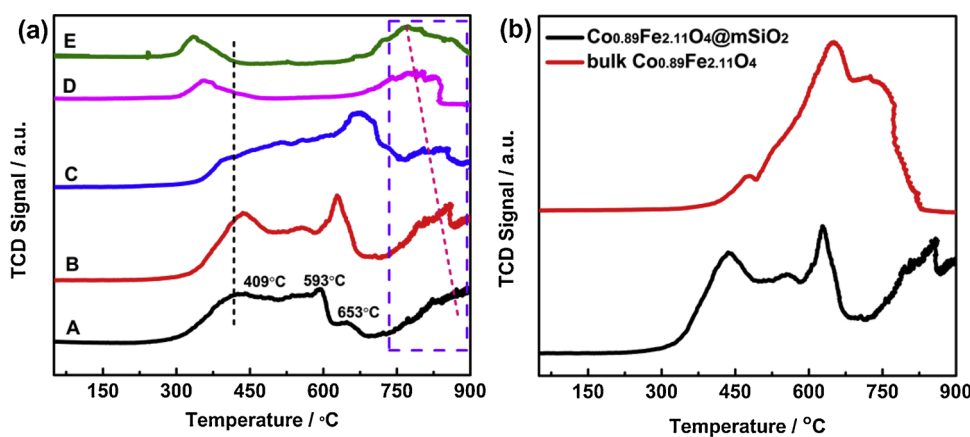

Fig. 8. (a) H_2-TPR profiles of (A) $Fe_2O_3@mSiO_2$, (B) $Co_{0.89}Fe_{2.11}O_4@mSiO_2$, (C) $Co_{1.67}Fe_{1.33}O_4@mSiO_2$, (D) $Co_{2.52}Fe_{0.48}O_4@mSiO_2$, and (E) $Co_3O_4@mSiO_2$ catalysts and H_2-TPR profiles of (b) $Co_{0.89}Fe_{2.11}O_4@mSiO_2@mSiO_2$ and bulk $Co_{0.89}Fe_{2.11}O_4$ catalysts.
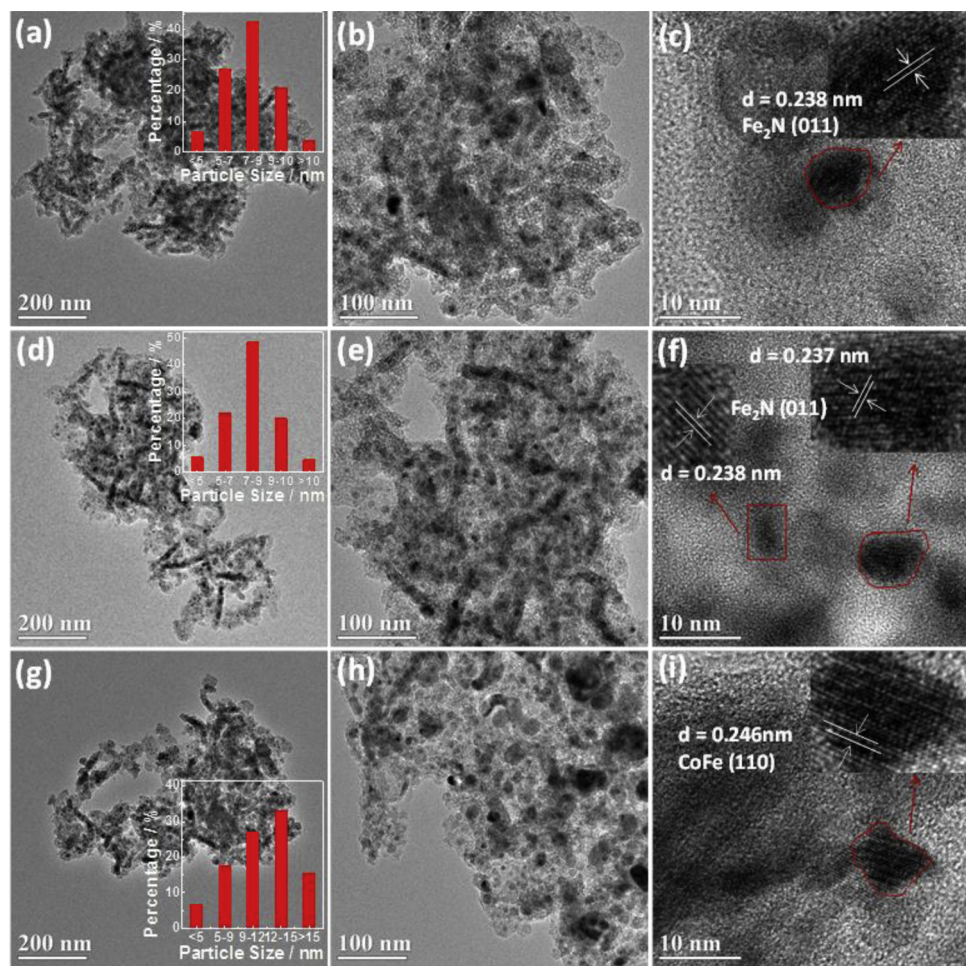
Fig. 9. TEM and HRTEM images of (a–c) Fe_2O_3@mSiO$_2$, (d–f) $Co_{0.89}Fe_{2.11}O_4$@mSiO$_2$, and (g–i) $Co_{2.52}Fe_{0.48}O_4$@mSiO$_2$ catalysts after the catalytic performance of NH$_3$ decomposition.
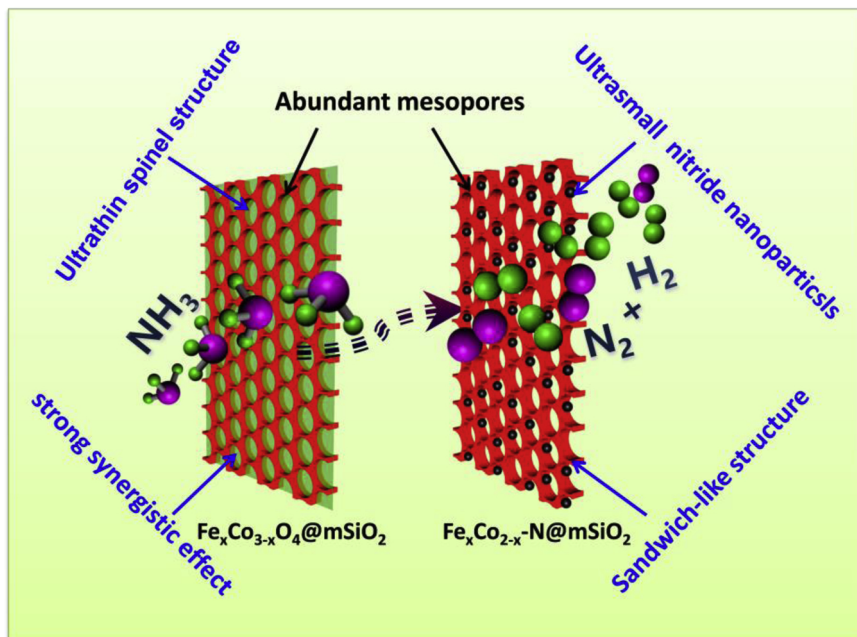
Scheme 2. The proposed mechanism for the improvement of NH$_3$ decomposition performance of $Co_xFe_{3-x}O_4$@mSiO$_2$ catalysts.

findings are expected to provide a feasible route for fabrication of spinel oxides nanocatalysts protected by mesoporous SiO$_2$ shells for catalyzing various reactions.

Acknowledgments

Appendix A. Supplementary data

Supplementary material related to this article can be found, in the online version, at doi:https://doi.org/10.1016/j.apcatb.2019.04.053.

References

[1] J. Chow, R.J. Kopp, P.R. Portney, Energy resources and global development, Science 302 (2003) 1528–1531.

[2] T.R. Cook, D.K. Dogutan, S.Y. Reece, Y. Surendranath, T.S. Teets, D.G. Nocera, Solar energy supply and storage for the legacy and nonlegacy worlds, Chem. Rev. 110 (2010) 6474–6502.

[3] F. Schüth, R. Palkovits, R. Schlögl, D.S. Su, Ammonia as a possible element in an energy infrastructure: catalysts for ammonia decomposition, Energy Environ. Sci. 5 (2012) 6278–6289.

[4] Y. Zhang, W. Qiu, Y. Ma, Y. Luo, Z. Tian, G. Cui, F. Xie, T. L. Chen, X. Li, Sun, High-performance electrohydrogenation of N$_2$ to NH$_3$ catalyzed bymultishelled hollow Cr$_2$O$_3$ microspheres under ambient conditions, ACS Catal. 8 (2018) 8540–8544.

[5] Y.-Q. Gu, Z. Jin, H. Zhang, R.-J. Xu, M.-J. Zheng, Y.-M. Guo, Q.-S. Song, C.-J. Jia, Transition metal nanoparticles dispersed in an alumina matrix as active and stable catalysts for Co$_x$-free hydrogen production from ammonia, J. Mater. Chem. A 3 (2015) 17172–17180.

[6] P. Yu, J. Guo, L. Liu, P. Wang, G. Wu, F. Chang, P. Chen, Ammonia decomposition with manganese nitride–calcium imide composites as efficient catalysts, ChemSusChem 9 (2016) 364–369.

[7] X. Jua, L. Liu, P. Yu, J. Guo, X. Zhang, T. He, G. Wu, P. Chen, Mesoporous Ru/MgOprepared by a deposition-precipitation method as highly active catalyst for producing Co$_x$-free hydrogen from ammonia decomposition, Appl. Catal. B: Environ. 211 (2017) 167–175.

[8] S. Zhou, S. Lin, H. Guo, First-principles insights into ammonia decomposition catalyzed by Ru clusters anchored on carbon nanotubes: size dependence andinterfacial effects, J. Phys. Chem. C122 (2018) 9091–9100.

[9] S. Mukherjee, S.V. Devaguptapu, A. Sviripa, C.R.F. Lund, G. Wu, Low-temperature ammonia decomposition catalysts for hydrogen generation, Appl. Catal. B: Environ. 226 (2018) 162–181.

[10] V. Tagliazucca, K. Schlichte, F. Schüth, C. Weidenthaler, Molybdenum-based catalysts for the decomposition of ammonia: in situ x-ray diffraction studies, microstructure, and catalytic properties, J. Catal. 305 (2013) 277–289.

[11] A. Srifa, K. Okura, T. Okanishi, H. Muroyama, T. Matsui, K. Eguchi, Hydrogenproduction by ammonia decomposition over Cs-modified Co$_3$Mo$_3$Ncatalysts, Appl. Catal. B: Environ. 218 (2017) 1–8.

[12] J.-Q. Zhong, X. Zhou, K. Yuan, C.A. Wright, A. Tadich, D. Qi, H.X. Li, K. Wu, G.Q. Xu, W. Chen, Probing the effect of the Pt–Ni–Pt(111) bimetallic surface electronic structures on the ammonia decomposition reaction, Nanoscale 9 (2017) 666–672.

[13] K. Obata, K. Kishishita, A. Okemoto, K. Taniya, Y. Ichihashi, S. Nishiyama, Photocatalytic decomposition of NH$_3$ over TiO$_2$catalysts doped with Fe, Appl. Catal. B: Environ 160−161 (2014) 200–203.

[14] S. Hajduka, V.D.B.C. Dasireddy, B. Likozar, G. Drazi, Z.C. Orela, CO$_x$-freehydrogen production via decomposition of ammonia over Cu–Zn-basedheterogeneous catalysts and their activity/stability, Appl. Catal. B: Environ. 211 (2017) 57–67.

[15] G. Li, H. Nagasaw, M. Kanezashi, T. Yoshioka, T. Tsuru, Graphene nanosheets supporting Ru nanoparticles with controlled nanoarchitectures form a high-performance catalyst for CO$_x$-free hydrogen production from ammonia, J. Mater. Chem. A 2 (2014) 9185–9192.

[16] A.M. Karim, V. Prasad, G. Mpourmpakis, W.W. Lonergan, A.I. Frenkel, J.G. Chen, D.G. Vlachos, Correlating particle size and shape of supported Ru/γ-Al$_2$O$_3$catalysts with nh$_3$ decomposition activity, J. Am. Chem. Soc. 131 (2009) 12230–12239.

[17] A.-H. Lu, J.-J. Nitz, M. Comotti, C. Weidenthaler, K. Schlichte, C.W. Lehmann, O. Terasaki, F. Schüth, Spatially and size selective synthesis of fe-based nanoparticles on ordered mesoporous supports as highly active and stable catalysts for ammonia decomposition, J. Am. Chem. Soc. 132 (2010) 14152–14162.

[18] D. Varíslia, C. Korkusuz, T. Dogu, Microwave-assisted ammonia decomposition reaction over iron incorporated mesoporous carbon catalysts, Appl. Catal. B: Environ. 201 (2017) 370–380.

[19] L. Li, R. Jiang, W. Chu, H. Cang, H. Chen, J. Yan, Cobalt nanoparticles embedded in a porous carbon matrix as an efficient catalyst for ammonia decomposition, Catal. Sci. Technol. 7 (2017) 1363–1371.

[20] J. Zhang, M. Comotti, F. Schüth, R. Schlögl, D.S. Su, Commercial Fe- or Co-containing carbon nanotubes as catalysts for NH$_3$decomposition, Chem. Commun. 19 (2007) 1916–1918.

[21] D.A. Hansgen, D.G. Vlachos, J.G. Chen, Using first principles to predict bimetallic catalysts for the ammonia decomposition reaction, Nat. Chem. 2 (2010) 484–489.

[22] Q. Su, L. Gu, Y. Yao, J. Zhao, W. Jia, W. Ding, C.-T. Au, Layered double hydroxides derived Ni$_x$(Mg$_y$Al$_z$O$_n$) catalysts:enhanced ammonia decomposition by hydrogen spillover effect, Appl. Catal. B: Environ. 201 (2017) 451–460.

[23] W. Zheng, T.P. Cotter, P. Kaghazchi, T. Jacob, B. Frank, K. Schlichte, W. Zhang, D.S. Su, F. Schüth, R. Schlögl, Experimental and theoretical investigation of molybdenum carbide and nitride as catalysts for ammonia decomposition, J. Am. Chem. Soc. 135 (2013) 3458–3464.

[24] K. Li, R. Zhang, R. Gao, G.-Q. Shen, L. Pan, Y. Yao, K. Yu, X. Zhang, J.-J. Zou, Metal-defected spinel Mn$_x$Co$_{3-x}$O$_4$ with octahedral mn-enriched surface for highly efficient oxygen reduction reaction, Appl. Catal. B: Environ. 244 (2019) 536–545.

[25] Q. Zhao, Z. Yan, C. Chen, J. Chen, Spinels: controlled preparation, oxygen reduction/evolution reaction application, and beyond, Chem. Rev. 117 (2017) 10121–10211.

[26] X. Cao, J. Wu, C. Jin, J. Tian, P. Strasser, R. Yang, MnCo$_2$O$_4$anchored on p-doped hierarchical porous carbon as an electrocatalyst for high-performance rechargeable Li–O$_2$batteries, ACS Catal. 5 (2015) 4890–4896.

[27] J. Xiong, Q. Wu, X. Mei, J. Liu, Y. Wei, Z. Zhao, D. Wu, J. Li, Fabrication of spinel-type Pd$_x$Co$_{3-x}$O$_4$binary active sites on 3d ordered meso-macroporous Ce-ZrO$_2$ with enhanced activity for catalytic soot oxidation, ACS Catal. 8 (2018) 7915–7930.

[28] C. Li, X. Han, F. Cheng, Y. Hu, C. Chen, J. Chen, Phase and composition controllable synthesis of cobalt manganese spinel nanoparticles towards efficient oxygen electrocatalysis, Nat. Commun. 6 (2015) 7345.

[29] Q. He, K. Rui, C. Chen, J. Yang, Z. Wen, Interconnected CoFe$_2$O$_4$–polypyrrole nanotubes as anode materials for high performance sodium ion batteries, ACS Appl. Mater. Interfaces 9 (2017) 36927–36935.

[30] L. Zhang, T. Wei, Z. Jiang, C. Liu, H. Jiang, J. Chang, L. Sheng, Q. Zhou, L. Yuan, Z. Fan, Electrostatic interaction in electrospun nanofibers: double-layer carbon protection of CoFe$_2$O$_4$nanosheets enabling ultralong-life and ultrahigh-rate lithium ion storage, Nano Energy 48 (2018) 238–247.

[31] Y. Zhang, L. Shen, M. Liu, X. Li, X. Lu, L. Lu, C. Ma, C. You, A. Chen, C. Huang, L. Chen, M. Alexe, C.-L. Jia, Flexible quasi-two-dimensional CoFe$_2$O$_4$ epitaxial thin films for continuous strain tuning of magnetic properties, ACS Nano 11 (2017) 8002–8009.

[32] H. Zhang, Ultrathin two-dimensional nanomaterials, ACS Nano 9 (2015) 9451–9469.

[33] C. Tan, H. Zhang, Wet-chemical synthesis and applications of non-layer structured two-dimensional nanomaterials, Nat. Commun. 6 (2015) 7873.

[34] C. Tan, H. Zhang, Epitaxial growth of hetero-nanostructures based on ultrathin two-dimensional nanosheets, J. Am. Chem. Soc. 137 (2015) 12162–12174.

[35] K. Xu, P. Chen, X. Li, Y. Tong, H. Ding, X. Wu, W. Chu, Z. Peng, C. Wu, Y. Xie, Metallic nickel nitride nanosheets realizing enhanced electrochemical water oxidation, J. Am. Chem. Soc. 137 (2015) 4119–4125.

[36] Y. Sun, Z. Sun, S. Gao, H. Cheng, Q. Liu, J. Piao, T. Yao, C. Wu, S. Hu, S. Wei, Y. Xie, Fabrication of flexible and freestanding zinc chalcogenide single layers, Nat. Commun. 3 (2012) 1057.

[37] G. Fan, F. Li, D.G. Evans, X. Duan, Catalytic applications of layered double hydroxides: recent advances and perspectives, Chem. Soc. Rev. 43 (2014) 7040–7066.

[38] X. Jia, Y. Zhao, G. Chen, L. Shang, R. Shi, X. Kang, G.I.N. Waterhouse, L.-Z. Wu, C.-H. Tung, T. Zhang, Ni$_3$FeN nanoparticles derived from ultrathin nife–layered double hydroxide nanosheets: an efficient overall water splitting electrocatalyst, Adv. Energy Mater. 6 (2016) 1502585.

[39] Y. Zhao, G. Chen, T. Bian, C. Zhou, G.I. Waterhouse, L.Z. Wu, C.H. Tung, L.J. Smith, D. O'Hare, T. Zhang, Defect-rich ultrathinZnAl-layered double hydroxide nanosheets for efficient photoreduction of CO$_2$ to CO with water, Adv. Mater. 27 (2015) 7824–7831.

[40] Q. Wang, D. O'Hare, Recent advances in the synthesis and application of layered double hydroxide (LDH) nanosheets, Chem. Rev. 112 (2012) 4124–4155.

[41] X. Gong, Y.-Q. Gu, N. Li, H. Zhao, C.-J. Jia, Y. Du, Thermally stable hierarchical nanostructures of ultrathin MoS$_2$nanosheet-coated CeO$_2$ hollow spheres as catalyst for ammonia decomposition, Inorg. Chem. 55 (2016) 3992–3999.

[42] L. Shang, T. Bian, B. Zhang, D. Zhang, L.-Z. Wu, C.-H. Tung, Y. Yin, T. Zhang, Graphene-supported ultrafine metal nanoparticles encapsulated by mesoporous silica: robust catalysts for oxidation and reduction reactions, Angew. Chem. Int. Ed. 53 (2014) 250–254.

[43] K. Zhang, W. Wang, L. Kuai, B. Geng, A facile and efficient strategy to gram-scale preparation of composition-controllable Ni-Fe LDHs nanosheets for superior OER Catalysis, Electrochim. Acta 225 (2017) 303–309.

[44] Q. Song, Z.J. Zhang, Controlled synthesis and magnetic properties of bimagnetic spinel ferrite CoFe$_2$O$_4$ and MnFe$_2$O$_4$nanocrystals with core-shell architecture, J. Am. Chem. Soc. 134 (2012) 10182–10190.

[45] L. Huo, B. Liu, G. Zhang, J. Zhang, Universal strategy to fabricate a two-dimensional layered mesoporous Mo$_2$C electrocatalyst hybridized on graphene sheets with high activity and durability for hydrogen generation, ACS Appl. Mater. Interfaces 8 (2016) 18107–18118.

[46] H. Wang, C. Chen, Y. Zhang, L. Peng, S. Ma, T. Yang, H. Guo, Z. Zhang, D.S. Su, J. Zhang, In situ oxidation of carbon-encapsulated cobalt nanocapsules creates highly active cobalt oxide catalysts for hydrocarbon combustion, Nat. Commun. 6 (2015) 7181.

[47] L. Wang, Y. Yi, Y. Zhao, R. Zhang, J. Zhang, H. Guo, NH$_3$decomposition for h$_2$ generation: effects of cheap metals and supports on plasma−catalyst synergy, ACS Catal. 5 (2015) 4167–4174.

[48] I. Nakamura, T. Fujitani, Role of metal oxide supports in NH$_3$decomposition over Ni

catalysts, Appl. Catal. A Gen. 524 (2016) 45–49.

[49] Z. Zhang, W. Li, R. Zou, W. Kang, Y.S. Chui, M.F. Yuen, C.-S. Lee, W. Zhang, Layer-stacked cobalt ferrite (CoFe$_2$O$_4$) mesoporous platelets for high-performance lithium ion battery anodes, J. Mater. Chem. A 3 (2015) 6990–6997.

[50] C. Wang, H. Su, Y. Ma, D. Yang, Y. Dong, D. Li, L. Wang, Y. Liu, J. Zhang, Coordination polymers-derived three-dimensional hierarchical CoFe$_2$O$_4$ hollow spheres as high-performance Lithium ion storage, ACS Appl. Mater. Interfaces 10 (2018) 28679–28685.

[51] Y. Kim, J.H. Park, J.G. Kim, Y. Noh, Y. Kim, H. Han, W.B. Kim, Ruthenium oxide incorporated one-dimensional cobalt oxide composite nanowires as lithium-oxygen battery cathode catalysts, ChemCatChem 9 (2017) 3554–3562.

[52] Y. Zhang, J. Huang, Y. Ding, Porous Co$_3$O$_4$/CuO hollow polyhedral nanocages derived from metal-organic frameworks with heterojunctions as efficient photocatalytic water oxidation catalysts, Appl. Catal. B: Environ. 198 (2016) 447–456.

[53] R.D.L. Smith, M.S. Prévot, R.D. Fagan, S. Trudel, C.P. Berlinguette, Water oxidation catalysis: electrocatalytic response to metal stoichiometry in amorphous metal oxide films containing iron, cobalt, and nickel, J. Am. Chem. Soc. 135 (2013) 11580–11586.

[55] A. Biabani-Ravandi, M. Rezaei, Low temperature CO oxidation over Fe–Co mixed oxide nanocatalysts, Chem. Eng. J. 184 (2012) 141–146.

[56] Y. Wang, D. Liu, Z. Liu, C. Xie, J. Huo, S. Wang, Porous cobalt–iron nitride nanowires as excellent bifunctional electrocatalysts for overall water splitting, Chem. Commun. 52 (2016) 12614–12617.

[57] X. Chen, J. Zhang, X. Fu, M. Antonietti, X. Wang, Fe-g-C$_3$N$_4$-catalyzed oxidation of benzene to phenol using hydrogen peroxide and visible light, J. Am. Chem. Soc. 131 (2009) 11658–11659.

[58] D. Yang, T. Jiang, T. Wu, P. Zhang, H. Han, B. Han, Highly selective oxidation of cyclohexene to 2-cyclohexene-1-one in water using molecular oxygen over Fe–Co–g-C$_3$N$_4$, Catal. Sci. Technol. 6 (2016) 193–200.